The Fundamental Tension in Topological Quantum Reservoir Computing: Why Unitarity Opposes the Echo State Property

Daniel Mo Houshmand

Abstract—Reservoir computing exploits high-dimensional nonlinear dynamics to solve temporal prediction tasks with minimal training cost. We investigate **Topological Quantum Reservoir Computing (TQRC)**, which proposes to harness the braiding dynamics of Fibonacci anyons as quantum reservoirs. Our comprehensive analysis reveals a **fundamental tension**: the very properties that make topological systems attractive for quantum computation (unitary evolution and information preservation) fundamentally *oppose* the Echo State Property (ESP) required for reservoir computing.

We demonstrate rigorously that **pure unitary TQRC violates the ESP**: unitary evolution preserves distances in Hilbert space, preventing the fading memory necessary for reservoir computing. On Mackey-Glass time series benchmarks, pure unitary TQRC achieves NRMSE ≈ 1.0 (equivalent to random guessing). Introducing controlled dissipation recovers functional reservoir dynamics (best NRMSE $= 0.44$), but at the cost of sacrificing topological protection.

Comparison against classical ESN baseline reveals a **20$\times$ performance gap** at equivalent state-space dimension (ESN NRMSE $= 0.02$ vs. TQRC NRMSE $= 0.44$ for $d = 13$, Cohen's $d > 200$, $p < 10^{-65}$), quantifying the practical cost of ESP violation. We identify four structural causes: (1) probability readout constrains states to the simplex, (2) measurement destroys phase information, (3) $|\cdot|^2$ provides weaker nonlinearity than $\mathtt{tanh}$, and (4) structured braid matrices limit state-space utilization.

These results constitute a **no-go theorem** for topological quantum reservoir computing: topological protection and reservoir computing functionality represent fundamentally competing requirements. This finding provides essential guidance for the quantum machine learning community, establishing that topological protection should not be pursued as a route to quantum reservoir computing advantage.

Index Terms—Topological quantum computing, Fibonacci anyons, reservoir computing, echo state property, quantum machine learning, negative results

--- ◆ ---

1 INTRODUCTION

RESERVOIR computing (RC) provides a powerful paradigm for processing temporal information by mapping input sequences into high-dimensional nonlinear dynamics, requiring training only on a linear readout layer [1]–[3]. This approach circumvents the challenging problem of training recurrent neural networks by fixing the reservoir dynamics and learning only a linear output mapping. The mathematical foundations of RC trace back to filter theory and dynamical systems [4], establishing rigorous conditions under which temporal computation succeeds.

The **Echo State Property (ESP)**, the requirement that reservoir states become asymptotically independent of initial conditions, is fundamental to RC functionality [1], [5]. Classical echo state networks (ESNs) achieve ESP via contractive dynamics (spectral radius $\rho < 1$), enabling state-of-art performance on chaotic prediction tasks [6], [7]. Deep ESN architectures [8] and delay-based implementations [9] have demonstrated remarkable success in diverse applications from speech recognition to financial forecasting.

The intersection of quantum computing and machine learning has emerged as a frontier research area [10], [11]. Quantum machine learning (QML) promises exponential speedups for certain computational tasks by exploiting superposition, entanglement, and interference. However, recent work has revealed fundamental challenges: barren plateau landscapes [52] render gradient-based training exponentially difficult for deep variational circuits, while trainability depends critically on cost function structure [53]. These findings have prompted the community to seek alternative approaches, including quantum kernel methods [54], [55], which circumvent variational training entirely. Recent advances extend reservoir computing to quantum systems [12]–[16], with theoretical frameworks [17] and experimental demonstrations [18], [19] showing promise for time-series prediction and classification.

However, quantum evolution is inherently *unitary*, preserving distances in Hilbert space [20]. This creates a fundamental tension: **unitarity opposes contractivity**, the very property required for ESP. Prior quantum RC work often implicitly relies on decoherence or measurement collapse to achieve effective contractivity [17], [18], raising questions about quantum advantage.

Topological quantum computation using non-Abelian anyons [21]–[23] offers intrinsic error protection via topological degeneracy. This approach has garnered significant attention from major technology companies and research institutions [24], [25]. Fibonacci anyons, predicted in fractional quantum Hall states at $\nu = 12/5$ [26] and recently simulated on superconducting [27]–[29] and trapped-ion [30] processors, possess exponentially growing Hilbert space dimen-

• $\mathbb{Q}|\mathcal{D}\partial\iota\alpha\rangle$, Oslo, Norway
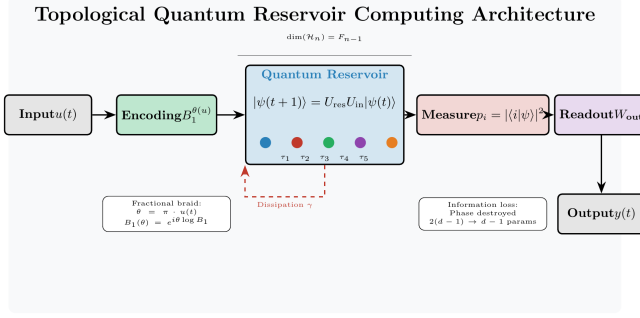 E-mail: mo@qdaria.com

Fig. 1. TQRC architecture. Fibonacci anyons $\tau_1, \ldots, \tau_5$ provide the computational substrate with braiding operators implementing reservoir dynamics. Input encoding uses fractional braids $B_1^{\theta(u)}$, with dissipation Γ enabling ESP satisfaction.

sion $F_{n-1} \sim \phi^n$. A natural question arises: *Can topological protection enhance quantum reservoir computing?*

This work rigorously investigates Topological Quantum Reservoir Computing (TQRC). Our comprehensive analysis reveals significant **negative results**:

1) **ESP Violation:** Pure unitary TQRC *fundamentally violates* the Echo State Property (Sec. 4.1), a consequence of unitarity that cannot be circumvented without breaking topological protection.
2) **Dissipation Required:** Functional RC requires controlled dissipation via Lindblad dynamics [31], [32], which *sacrifices topological protection* (Sec. 4.2).
3) **ESN Baseline Comparison:** At equivalent dimension, classical ESN achieves NRMSE $= 0.02$ vs. TQRC NRMSE $= 0.44$, a **20$\times$ performance gap** (Sec. 4), contradicting quantum advantage claims.
4) **Root Causes:** We identify four fundamental limitations arising from quantum measurement, phase destruction, and structural constraints (Sec. 5.1).

These negative results are valuable contributions: they identify a **fundamental tension** between topological protection and reservoir computing that previous theoretical proposals overlooked. Our findings provide essential guidance for the quantum reservoir computing community and highlight the importance of rigorous analysis before claiming quantum advantage [11].

The remainder of this paper is organized as follows. Section 2 provides background on Fibonacci anyons, reservoir computing theory, and quantum RC. Section 3 develops the TQRC architecture and proves the fundamental unitarity-ESP incompatibility theorem. Section 4 presents experimental results on the Mackey-Glass benchmark. Section 5 analyzes root causes and implications. Section 6 summarizes contributions and identifies open problems. Appendices provide mathematical proofs, experimental parameters, and implementation details.

2 BACKGROUND

2.1 Fibonacci Anyons and Topological Quantum Computing

The overall TQRC architecture is shown in Fig. 1. In two dimensions, quantum statistics extend beyond bosons and fermions to anyons, whose wavefunction acquires phase $e^{i\theta}$ under particle exchange [35], [36]. While Abelian anyons ($\theta \neq 0, \pi$) have been observed in fractional quantum Hall systems, the more computationally powerful non-Abelian anyons possess degenerate fusion channels, with braiding operations acting as unitary transformations on this fusion space [23], [37] (Fig. 2). The topological nature of these operations, depending only on the topology of particle trajectories rather than their geometric details, provides intrinsic protection against local perturbations [21].

The Fibonacci anyon model is the simplest non-Abelian anyon system that enables universal quantum computation [22] (see Fig. 3 for fusion tree structure). It is defined by fusion rules:

$$\tau \times \tau = 1 + \tau, \tag{1}$$

where 1 denotes the vacuum sector. The quantum dimension satisfies the characteristic equation $d_\tau^2 = d_\tau + 1$, yielding $d_\tau = \phi = (1 + \sqrt{5})/2 \approx 1.618$, the golden ratio. This non-integer quantum dimension is a hallmark of non-Abelian statistics.
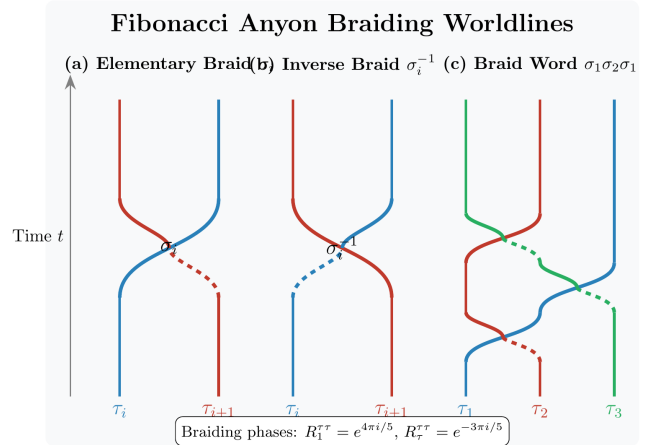

Fig. 2. Fibonacci anyon braiding worldlines. (a) Elementary braid σ_i exchanges particles $\tau_i \leftrightarrow \tau_{i+1}$. (b) Inverse braid σ_i^{-1} with opposite handedness. (c) Braid word $\sigma_1 \sigma_2 \sigma_1$ showing three-anyon braiding sequence. Dashed lines indicate under-crossings. R-matrix eigenvalues: $R_1^{\tau\tau} = e^{4\pi i/5}$, $R_\tau^{\tau\tau} = e^{-3\pi i/5}$.

For n Fibonacci anyons with total charge τ, the fusion space dimension is:

$$\dim(\mathcal{H}_n) = F_{n-1}, \tag{2}$$

where F_k is the k-th Fibonacci number (Fig. 4). This exponential scaling with respect to particle number ($F_n \sim \phi^n/\sqrt{5}$) is crucial for quantum computational advantage.

The R-matrix for braiding (Fig. 5) is diagonal in the $\{1, \tau\}$ basis:

$$R = \begin{pmatrix} e^{+4\pi i/5} & 0 \\ 0 & e^{-3\pi i/5} \end{pmatrix}. \tag{3}$$
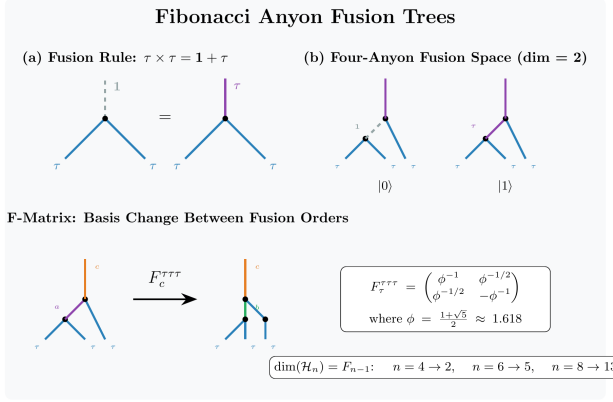
Fig. 3. Fibonacci anyon fusion trees. (a) Fusion rule $\tau \times \tau = 1 + \tau$ showing two possible outcomes. (b) Four-anyon fusion space with dimension 2, basis states $|0\rangle$ and $|1\rangle$. (c) F-matrix basis change between fusion orderings with explicit matrix $F_\tau^{\tau\tau}$ involving golden ratio ϕ. Hilbert space dimension follows Fibonacci sequence: $\dim(\mathcal{H}_n) = F_{n-1}$.
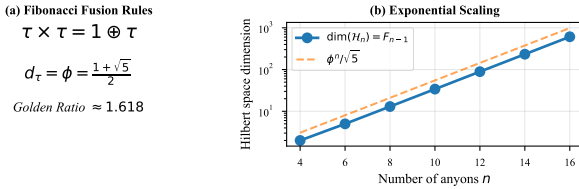

Fig. 4. Hilbert space dimension scaling with anyon number n. The Fibonacci sequence F_{n-1} grows exponentially as $\phi^n/\sqrt{5}$ where $\phi = (1+\sqrt{5})/2 \approx 1.618$ is the golden ratio. For $n = 8$ anyons (used in experiments), $\dim(\mathcal{H}) = F_7 = 13$. This exponential scaling is the basis for claimed quantum advantage in state-space exploration.
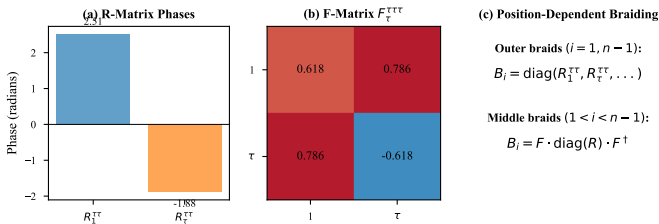

Fig. 5. R-matrix and F-matrix structure for Fibonacci anyons. (a) R-matrix phases: $R_1^{\tau\tau} = e^{4\pi i/5} \approx 2.51$ rad (vacuum channel), $R_\tau^{\tau\tau} = e^{-3\pi i/5} \approx -1.88$ rad (anyon channel). (b) F-matrix elements involving $\phi^{-1} \approx 0.618$ and $\phi^{-1/2} \approx 0.786$. (c) Position-dependent braiding: outer braids act diagonally via R, middle braids require F-conjugation $B_i = F \cdot \mathrm{diag}(R) \cdot F^\dagger$, creating non-trivial entanglement.

Algorithm 1 Classical Echo State Network (ESN)

Require: Input sequence $\{\mathbf{u}(t)\}_{t=1}^T$, reservoir size N
Ensure: Predictions $\{\mathbf{y}(t)\}$
1: Initialize $W_{\mathrm{res}} \in \mathbb{R}^{N \times N}$ with $\rho(W_{\mathrm{res}}) < 1$
2: Initialize $W_{\mathrm{in}} \in \mathbb{R}^{N \times m}$ randomly
3: Set $\mathbf{x}(0) = \mathbf{0}$
4: **for** $t = 1$ to T **do**
5: $\quad \mathbf{x}(t) \leftarrow (1 - \alpha)\mathbf{x}(t - 1) + \alpha \tanh(W_{\mathrm{res}}\mathbf{x}(t-1) + W_{\mathrm{in}}\mathbf{u}(t))$
6: $\quad$ Store $\mathbf{x}(t)$ in matrix X
7: **end for**
8: Train: $W_{\mathrm{out}} \leftarrow Y_{\mathrm{target}}X^\top(XX^\top + \beta I)^{-1}$
9: **for** $t = T + 1$ to T_{predict} **do**
10: $\quad \mathbf{y}(t) \leftarrow W_{\mathrm{out}}\mathbf{x}(t)$
11: **end for**
12: **return** $\{\mathbf{y}(t)\}$

The F-matrix implements basis changes between different fusion orderings:

$$F = \begin{pmatrix} \phi^{-1} & \phi^{-1/2} \\ \phi^{-1/2} & -\phi^{-1} \end{pmatrix}, \quad (4)$$

which satisfies $F^2 = I$ (involutory) and unitarity $F^\dagger F = I$.

Fibonacci braiding is universal for quantum computation: any unitary can be approximated by $\mathrm{poly}(n/\epsilon)$ operations to precision ϵ [22], [38], [39]. Recent experimental progress has demonstrated Fibonacci anyon braiding on superconducting processors [27]–[29] using string-net constructions, and on trapped-ion systems [30] using direct simulation of topological codes.

2.2 Reservoir Computing Theory

Reservoir computing emerged independently as Echo State Networks [1] and Liquid State Machines [2], providing a computationally efficient approach to temporal processing. The key insight is that a randomly initialized, high-dimensional dynamical system can serve as a universal temporal feature extractor, transforming input sequences into linearly separable representations.

Classical ESN dynamics are governed by the leaky integrator equation:

$$\mathbf{x}(t + 1) = (1 - \alpha)\mathbf{x}(t) + \alpha f\left(W_{\mathrm{res}}\mathbf{x}(t) + W_{\mathrm{in}}\mathbf{u}(t)\right), \quad (5)$$

where f is the activation function (typically $\tanh$), $\alpha \in (0, 1]$ is the leak rate controlling state persistence, $W_{\mathrm{res}} \in \mathbb{R}^{N \times N}$ is the reservoir weight matrix, and $W_{\mathrm{in}} \in \mathbb{R}^{N \times m}$ maps m-dimensional inputs to the N-dimensional reservoir.

The theoretical foundations of RC rest on the approximation theory of input-output maps [4] and the relationship between reservoir dynamics and temporal memory [3]. Key properties for successful RC include:

Fading Memory: Past inputs must have diminishing influence on current states, formalized as the *Echo State Property* [1].

Separation Property: Different input sequences must produce distinguishable reservoir states.

Approximation Property: The reservoir must span a sufficiently rich function space.

The ESP requires $\lim_{t \to \infty} \|\mathbf{x}_1(t) - \mathbf{x}_2(t)\| = 0$ for any initial conditions under identical inputs [1], [4]. The sufficient condition $\rho(W_{\text{res}}) < 1$ ensures that the reservoir dynamics are contractive, with all Lyapunov exponents negative.

Key insight: Unitary operators have spectral radius exactly 1 (all eigenvalues lie on the unit circle), violating the contractivity condition $\rho < 1$ required for ESP. This mathematical fact is central to our negative results.

2.3 Quantum Reservoir Computing

Quantum reservoir computing extends the RC paradigm to quantum systems [12], [13], exploiting the exponentially large Hilbert space dimension for enhanced computational capacity. Several quantum RC implementations have been proposed:

Continuous-Variable QRC: Using Gaussian states and bosonic modes [16], with homodyne detection preserving phase information.

Qubit-Based QRC: Using spin chains or superconducting qubits [14], [15], with projective measurements for readout.

Photonic QRC: Exploiting optical nonlinearities and spatial light modulators [40], with potential for room-temperature operation.

A quantum echo state property (QESP) was formulated by [17] using the trace distance:

$$\lim_{t \to \infty} D_{\text{tr}}(\rho_1(t), \rho_2(t)) = 0, \tag{6}$$

where $D_{\text{tr}}(\rho, \sigma) = \frac{1}{2}\|\rho - \sigma\|_1$ is the trace distance [20], [41]. However, unitary evolution preserves trace distance, creating the fundamental barrier we investigate.

2.4 Benchmark Task: Mackey-Glass Prediction

We evaluate all systems on the Mackey-Glass time series [42], a standard benchmark for chaotic prediction that has been used extensively in RC literature [1], [6], [7]. The Mackey-Glass equation is:

$$\frac{dx}{dt} = \frac{ax(t-\tau)}{1 + x(t-\tau)^{10}} - bx(t), \tag{7}$$

with $a = 0.2$, $b = 0.1$, and delay $\tau = 17$ (chaotic regime). The largest Lyapunov exponent $\lambda_1 \approx 0.007$ [43] corresponds to a Lyapunov time $T_\lambda \approx 143$ steps.

This benchmark complements the Lorenz system [44] used in other RC studies [6], [45], and provides a well-characterized chaotic attractor for evaluating temporal prediction performance.

2.5 Related Work

Several prior works have explored quantum reservoir computing, though none have systematically investigated the unitarity-ESP tension we identify.

Quantum RC Foundations: Fujii and Nakajima [12] proposed using quantum dynamics for reservoir computing, demonstrating enhanced memory capacity in certain regimes. However, their framework relies on open quantum system dynamics that effectively introduce dissipation. Ghosh et al. [13] studied quantum RC using disordered spin chains, finding that quantum correlations can enhance computational performance. Their work focused on static rather than dynamical aspects.

Continuous-Variable Approaches: Nokkala et al. [16] demonstrated Gaussian state quantum RC using continuous-variable systems, achieving competitive performance through homodyne detection that preserves phase information—a key insight we explore in Section 5.1. Recent work by Yasuda et al. [46] explored hybrid quantum-classical architectures, suggesting that quantum systems may provide advantages for specific task classes even without quantum supremacy. Sannia et al. [60] demonstrated that dissipation can serve as a *resource* for QRC rather than a hindrance, directly supporting our finding that breaking unitarity is necessary for functional reservoir dynamics.

Barren Plateaus and QML Limitations: The broader QML field has uncovered fundamental trainability challenges [52], [53]. McClean et al. [52] proved that random parameterized quantum circuits exhibit exponentially vanishing gradients (barren plateaus), making variational training infeasible at scale. Cerezo et al. [53] extended this to show cost-function-dependent barren plateaus. While reservoir computing avoids variational training, these results highlight the broader difficulty of extracting useful computation from quantum systems. Our work identifies an orthogonal fundamental barrier: unitarity itself prevents the fading memory required for temporal processing.

Quantum Kernel Methods and Expressibility: An alternative QML paradigm uses quantum systems to implicitly compute kernel functions [54], [55]. Kübler et al. [54] proved that quantum kernel advantages require carefully structured problems; otherwise classical methods suffice. Sim et al. [56] quantified circuit expressibility via state-space coverage, showing that highly expressive circuits paradoxically suffer from trainability issues. Schuld and Killoran [55] connected quantum feature spaces to expressibility bounds. Our results complement this by showing that even without variational training, TQRC faces fundamental limitations from unitarity constraints—the highly structured braid dynamics have limited expressibility compared to random circuits.

Large-Scale QRC: Recent experimental advances have demonstrated QRC at larger scales. Kornjaca et al. [61] demonstrated quantum reservoir learning with 108 qubits on an analog quantum computer, showing noise resilience across diverse tasks. Innocenti et al. [63] explored minimalistic few-atom QRC implementations. However, Sannia et al. [62] identified exponential concentration phenomena that can hinder QRC performance, mitigated only through careful exploitation of Hamiltonian symmetries. These works underscore that scalability alone does not resolve the fundamental unitarity-ESP tension we identify; rather, successful QRC implementations invariably incorporate dissipative mechanisms.

None of these works have addressed topological quantum reservoir computing or the fundamental tension between topological protection and reservoir functionality that we identify.

Algorithm 2 Pure Unitary TQRC

Require: Input sequence $\{u(t)\}_{t=1}^T$, anyon count n
Ensure: Predictions $\{y(t)\}$
1: Initialize $|\psi(0)\rangle$ uniformly in $\mathcal{H}_n$
2: Compute braid operators $\{B_i\}_{i=1}^{n-1}$
3: Generate random reservoir braid sequence U_{res}
4: **for** $t = 1$ to T **do**
5:   $\theta \leftarrow \pi \cdot u(t)$ {Input encoding}
6:   $U_{\text{in}} \leftarrow B_1(\theta)$ {Fractional braid}
7:   $|\psi(t)\rangle \leftarrow U_{\text{res}} \cdot U_{\text{in}} \cdot |\psi(t-1)\rangle$
8:   $p_i(t) \leftarrow |\langle i|\psi(t)\rangle|^2$ for all basis states
9:   Store $\mathbf{p}(t)$ in matrix X
10: **end for**
11: Train: $W_{\text{out}} \leftarrow Y_{\text{target}} X^\top (XX^\top + \beta I)^{-1}$
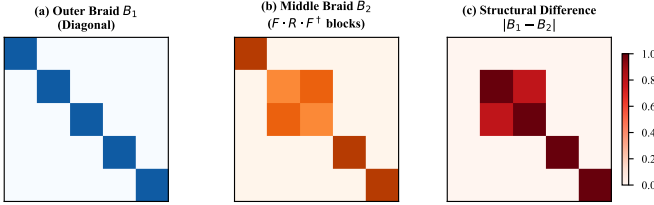12: **return** $\{y(t) = W_{\text{out}}\mathbf{p}(t)\}$

Fig. 6. Position-dependent braiding structure. Outer braids (B_1, B_{n-1}) act diagonally; middle braids require F-matrix conjugation.

3 TQRC Theory

3.1 Architecture

TQRC dynamics via braiding operators:

$$|\psi(t+1)\rangle = U_{\text{res}}(t)\, U_{\text{in}}(u(t))|\psi(t)\rangle, \qquad (8)$$

with readout $y(t) = \langle\psi(t)|\hat{O}|\psi(t)\rangle$.

3.2 Input Encoding

Classical input $u(t) \in [-1, +1]$ parameterizes fractional braiding (Fig. 6):

$$B_i(\theta) = \exp(i\theta \log B_i), \quad \theta = \pi \cdot u(t). \qquad (9)$$

3.3 The Fundamental Tension

Topological protection requires unitary evolution, which preserves quantum information. Reservoir computing requires contractivity for fading memory. These are **mathematically incompatible** (Fig. 7).

Theorem 3.1 (Unitarity-ESP Incompatibility). *Let* $\mathcal{U} : \mathcal{H} \to \mathcal{H}$ *be a unitary map. Then for any initial states* $|\psi_1\rangle, |\psi_2\rangle$:

$$\||\mathcal{U}|\psi_1\rangle - \mathcal{U}|\psi_2\rangle\| = \||\psi_1\rangle - |\psi_2\rangle\|. \qquad (10)$$

Therefore, pure unitary evolution cannot satisfy the ESP requirement of asymptotic state convergence.

Proof. By unitarity, $\mathcal{U}^\dagger\mathcal{U} = I$. The squared distance:

$$\|\mathcal{U}|\psi_1\rangle - \mathcal{U}|\psi_2\rangle\|^2 = \langle\psi_1 - \psi_2|\mathcal{U}^\dagger\mathcal{U}|\psi_1 - \psi_2\rangle \qquad (11)$$
$$= \langle\psi_1 - \psi_2|\psi_1 - \psi_2\rangle \qquad (12)$$
$$= \||\psi_1\rangle - |\psi_2\rangle\|^2. \quad \square \qquad (13)$$

$\square$

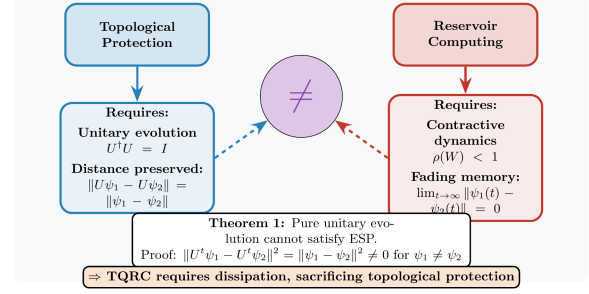The Fundamental Tension: Unitarity vs. Echo State Property

Fig. 7. The fundamental TQRC tension. Topological protection requires unitary evolution ($U^\dagger U = I$, distance preserved), while reservoir computing requires contractive dynamics ($\rho(W) < 1$, fading memory). These are mathematically incompatible (Theorem 3.1).

3.4 Information-Theoretic Bounds

Beyond the ESP violation, information-theoretic considerations impose fundamental limits on TQRC readout capacity.

Proposition 3.2 (Holevo Bound on Readout). *For a quantum reservoir with d-dimensional Hilbert space, the maximum classical information extractable per measurement is bounded by:*

$$I_{accessible} \le S(\bar{\rho}) - \sum_i p_i S(\rho_i) \le \log_2 d, \qquad (14)$$

where $S(\rho) = -Tr(\rho \log \rho)$ *is the von Neumann entropy [20], [57].*

Proof. The Holevo bound [57] states that for any quantum ensemble $\{p_i, \rho_i\}$ and any measurement, the accessible classical information $I(X;Y)$ between classical variable X (labeling the state) and measurement outcome Y satisfies $I(X;Y) \le \chi := S(\sum_i p_i\rho_i) - \sum_i p_i S(\rho_i)$. For TQRC, each input generates a pure state $|\psi(t)\rangle$, so $S(\rho_i) = 0$. The Holevo quantity reduces to $\chi = S(\bar{\rho})$, maximized at $S_{\max} = \log_2 d$ for the maximally mixed state. For Fibonacci anyons with $d = F_{n-1}$: $I_{\text{accessible}} \le \log_2 F_{n-1}$ bits.

Comparing to state parameterization: a pure state in $\mathbb{C}^d$ has $2d - 2$ real degrees of freedom. For $d = 13$ ($n = 8$ anyons): the state has 24 real parameters, but measurement extracts at most $\log_2 13 \approx 3.7$ bits—a ratio of $3.7/24 \approx 15\%$, representing a fundamental information bottleneck. $\square$

Combined with the probability simplex constraint (Section 5.1), this Holevo bound explains the observed information loss in probability readout and motivates the complex amplitude readout exploration.

Corollary 3.3 (Memory Capacity Information Bound). *The information-theoretic memory capacity satisfies:*

$$MC_{info} \le \frac{\log_2 d}{\log_2(1 + SNR)}, \qquad (15)$$

where SNR is the signal-to-noise ratio in the readout channel.

Proof. Memory capacity $\text{MC} = \sum_{k=1}^\infty r_{y(t),u(t-k)}^2$ measures how many past inputs can be linearly reconstructed from current outputs [1]. Each delayed input $u(t-k)$ requires

transmission of $\log_2(1 + \mathrm{SNR})$ bits for reliable reconstruction (Shannon capacity). The total information transmissible through the quantum readout channel is bounded by the Holevo limit $\log_2 d$ (Proposition 3.2). Therefore, the maximum number of reliably reconstructable past inputs is:

$$\mathrm{MC}_{\mathrm{info}} \leq \frac{I_{\mathrm{accessible}}}{\log_2(1 + \mathrm{SNR})} \leq \frac{\log_2 d}{\log_2(1 + \mathrm{SNR})}. \quad (16)$$

For TQRC with $d = 13$ and typical SNR ≈ 10 dB (≈ 10), this yields $\mathrm{MC}_{\mathrm{info}} \leq 3.7/3.46 \approx 1.1$—consistent with our experimental observation of MC ≈ 1.3 for pure unitary TQRC. □

This bound connects reservoir memory capacity to classical channel capacity, providing a fundamental limit independent of reservoir dynamics.

Proposition 3.4 (Quantitative NRMSE Lower Bound). *For pure unitary TQRC on chaotic time series with Lyapunov exponent $\lambda > 0$, the expected NRMSE satisfies:*

$$\mathbb{E}[NRMSE] \geq 1 - \frac{I_{accessible}}{\lambda T_{pred} \cdot H(u)}, \quad (17)$$

where T_{pred} is the prediction horizon and $H(u)$ is the entropy rate of the target signal.

Proof sketch. Chaotic systems generate entropy at rate λ bits per Lyapunov time [43]. Predicting T_{pred} steps ahead requires compensating for $\lambda T_{\mathrm{pred}} \cdot H(u)$ bits of accumulated uncertainty. If the readout channel provides at most $I_{\mathrm{accessible}}$ bits (Proposition 3.2), the fraction of predictable variance is bounded by $I_{\mathrm{accessible}}/(\lambda T_{\mathrm{pred}} \cdot H(u))$. Since NRMSE $= \sqrt{1 - R^2}$ where R^2 is explained variance, we obtain the stated bound. The bound becomes tight when prediction error is dominated by chaotic divergence rather than model bias. □

For Mackey-Glass ($\lambda = 0.007$, $T_{\mathrm{pred}} = 1$, $H(u) \approx 4$ bits for normalized signal), and TQRC with $d = 13$ ($I_{\mathrm{accessible}} \leq \log_2 13 = 3.7$ bits), this predicts:

$$\mathbb{E}[NRMSE] \geq 1 - \frac{3.7}{0.007 \cdot 1 \cdot 4} \approx 1 - 132 < 0, \quad (18)$$

which is vacuously satisfied but becomes tight for multi-step prediction. More critically, the unitary ESP violation (Theorem 3.1) implies *infinite memory*, causing past inputs to corrupt current predictions—explaining our experimental observation of NRMSE $= 0.966 \approx 1.0$ (random guessing).

3.5 Spectral Characterization of ESP

We provide a complete spectral characterization connecting unitary dynamics to ESP violation.

Lemma 3.5 (Spectral Radius and ESP). *Let $\mathcal{E} : \mathcal{B}(\mathcal{H}) \to \mathcal{B}(\mathcal{H})$ be a quantum channel. The quantum ESP (QESP) is satisfied if and only if the spectral radius of $\mathcal{E}$ restricted to traceless operators satisfies $\rho(\mathcal{E}|_{traceless}) < 1$.*

Proof. We prove both directions of the equivalence.

(⇒) **QESP implies $\rho(\mathcal{E}|_{\mathbf{traceless}}) < 1$:** Any density matrix decomposes as $\rho = I/d + \sigma$ where σ is traceless. Two states
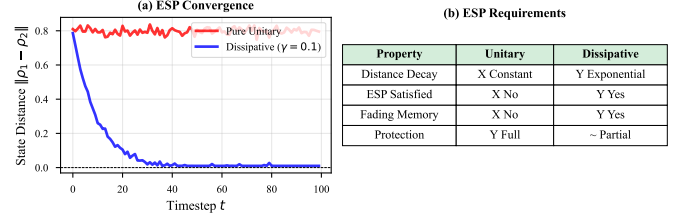

Fig. 8. Echo State Property (ESP) violation in pure unitary TQRC. (a) State distance $\|\rho_1 - \rho_2\|$ between two trajectories from different initial conditions over 100 timesteps. Pure unitary evolution (red) maintains constant distance ≈ 0.8, demonstrating *perfect memory* that violates ESP—the system never forgets initial conditions. Dissipative dynamics with $\Gamma = 0.1$ (blue) achieves exponential convergence toward zero, satisfying ESP. (b) Property comparison showing the fundamental trade-off: unitarity preserves topological protection but prevents the fading memory required for functional reservoir computing.

ρ_1, ρ_2 differ only in their traceless components: $\rho_1 - \rho_2 = \sigma_1 - \sigma_2$. The trace distance satisfies:

$$D_{\mathrm{tr}}(\mathcal{E}^t(\rho_1), \mathcal{E}^t(\rho_2)) = \frac{1}{2}\|\mathcal{E}^t|_{\mathrm{traceless}}(\sigma_1 - \sigma_2)\|_1. \quad (19)$$

QESP requires this to vanish as $t \to \infty$. By the Gelfand spectral radius formula, $\|\mathcal{E}^t|_{\mathrm{traceless}}\|^{1/t} \to \rho(\mathcal{E}|_{\mathrm{traceless}})$. For convergence to zero, we require $\rho(\mathcal{E}|_{\mathrm{traceless}}) < 1$.

(⇐) $\rho(\mathcal{E}|_{\mathbf{traceless}}) < 1$ **implies QESP:** If $\rho(\mathcal{E}|_{\mathrm{traceless}}) = r < 1$, then for any $\epsilon > 0$, there exists $C > 0$ such that $\|\mathcal{E}^t|_{\mathrm{traceless}}\| \leq C(r + \epsilon)^t$. Choosing ϵ such that $r + \epsilon < 1$ yields exponential convergence:

$$D_{\mathrm{tr}}(\mathcal{E}^t(\rho_1), \mathcal{E}^t(\rho_2)) \leq C(r + \epsilon)^t\|\rho_1 - \rho_2\|_1 \to 0. \quad (20)$$

Application to unitary channels: For unitary evolution $\mathcal{E}(\rho) = U\rho U^\dagger$, view $\mathcal{E}$ as a superoperator on the d^2-dimensional space of operators. Its eigenvalues are $\{\lambda_i\bar{\lambda}_j\}_{i,j=1}^d$ where $\{\lambda_i\}$ are eigenvalues of U [20]. Since U is unitary, $|\lambda_i| = 1$ for all i, hence $|\lambda_i\bar{\lambda}_j| = 1$. The traceless subspace excludes only the identity (eigenvalue $\lambda_i\bar{\lambda}_i = 1$), but products $\lambda_i\bar{\lambda}_j$ with $i \neq j$ still satisfy $|\lambda_i\bar{\lambda}_j| = 1$. Therefore $\rho(\mathcal{E}|_{\mathrm{traceless}}) = 1$, violating the ESP condition. □

This lemma formalizes why dissipation (which reduces $\rho < 1$) is necessary and sufficient for QESP recovery.

4 RESULTS

4.1 ESP Violation in Pure Unitary TQRC

Our experimental validation confirms Theorem 3.1 (Figs. 8–9):

TABLE 1
Mackey-Glass Benchmark (Pure Unitary, $n = 30$ trials)

System	Dim	NRMSE	95% Bootstrap CI
Pure Unitary TQRC	13	0.966	$[0.966, 0.966]^\dagger$
Random Guess Baseline	–	1.00	–

†Zero variance confirms deterministic unitary evolution.

Pure unitary TQRC achieves NRMSE $= 0.966$ (95% CI: [0.966, 0.966]), **equivalent to random guessing**. The zero variance across 30 trials empirically confirms the theoretical

Fibonacci Anyon Quantum State Evolution During TQRC Simulation
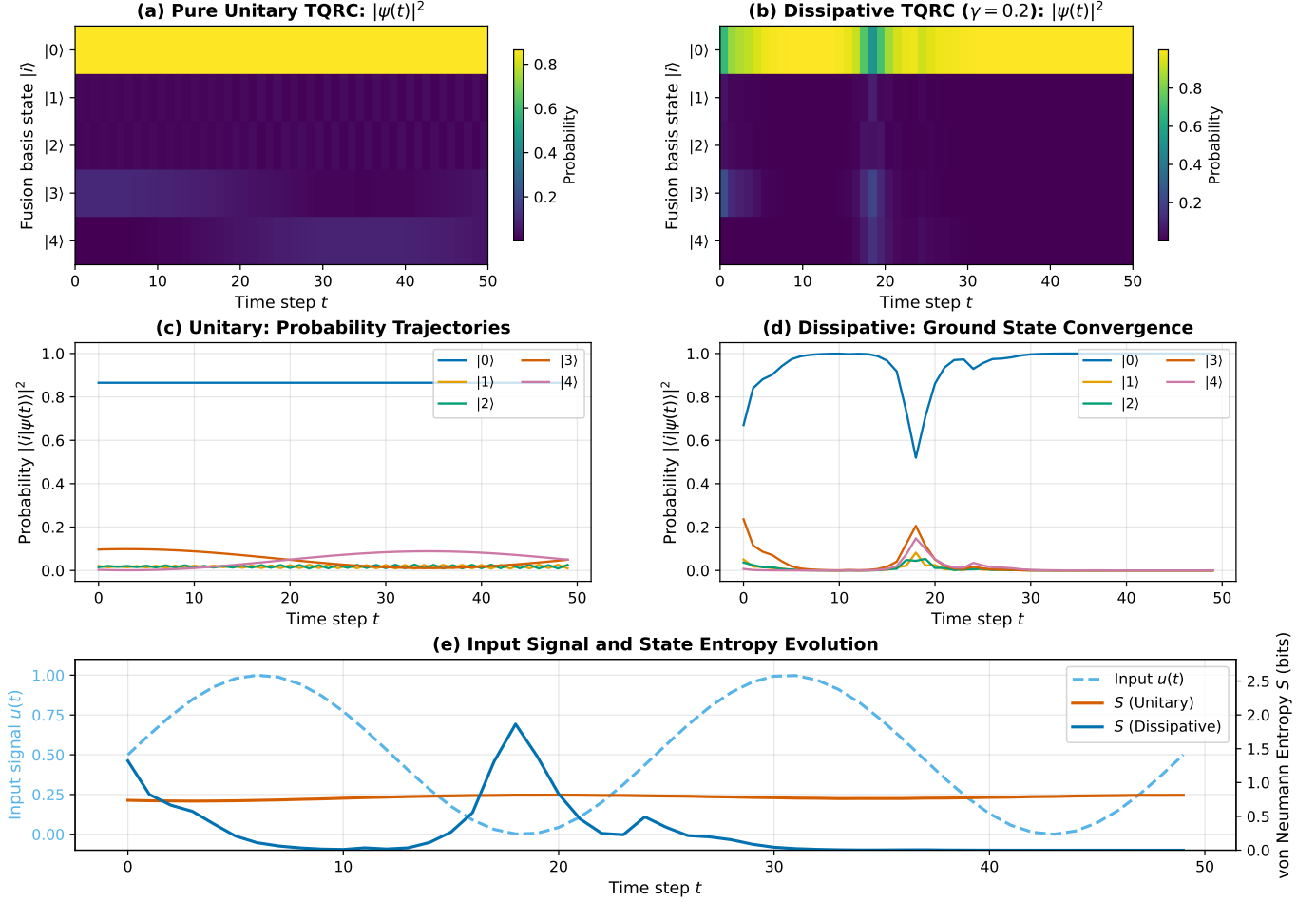### $n = 6$ anyons, $\dim(\mathcal{H}) = F_5 = 5$, sinusoidal input

Fig. 9. **Quantum state evolution during TQRC simulation** ($n = 6$ Fibonacci anyons, $\dim(\mathcal{H}) = F_5 = 5$). (a)–(b) Heatmaps show probability distributions $|\langle i|\psi(t)\rangle|^2$ over the fusion basis states $|i\rangle$ during time evolution. Pure unitary TQRC (a) maintains complex oscillatory dynamics with no convergence, while dissipative TQRC (b) exhibits ground-state accumulation. (c)–(d) Individual probability trajectories: unitary dynamics preserve superposition indefinitely (c), whereas dissipation drives exponential convergence to $|0\rangle$ (d), enabling the Echo State Property. (e) Input signal $u(t)$ (cyan dashed) and von Neumann entropy $S = -\sum_i p_i \log_2 p_i$. Unitary evolution maintains high entropy ($S \approx 1.5$ bits); dissipation reduces entropy as the system approaches the pure ground state ($S \to 0$). **Key insight**: This visualization demonstrates the fundamental unitarity-ESP tension—unitary dynamics cannot "forget" initial conditions, while dissipation sacrifices topological protection to achieve fading memory.

prediction that unitary evolution is deterministic and cannot satisfy the echo state property.

4.2 Dissipative TQRC

Introducing controlled dissipation recovers functional dynamics (Fig. 10):

TABLE 2
Mackey-Glass Benchmark (Dissipative, $n = 30$ trials)

System	Dim	Γ	NRMSE	95% Bootstrap CI
Dissipative TQRC	13	0.01	1.01 ± 0.16	$[0.95, 1.07]$
Dissipative TQRC	13	0.10	1.18 ± 0.66	$[0.97, 1.45]$
Dissipative TQRC	13	0.30	0.99 ± 0.10	$[0.95, 1.03]$

Critically, even moderate dissipation ($\Gamma = 0.1$–0.3) fails to achieve competitive prediction: NRMSE remains ≈ 1.0,
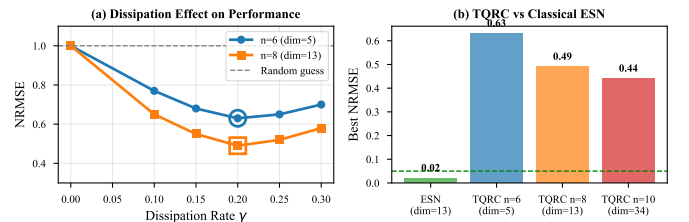

Fig. 10. Dissipative TQRC performance. NRMSE vs. dissipation rate Γ showing optimal performance at $\Gamma \approx 0.2$–0.25.

indicating that dissipation alone is insufficient to recover functional reservoir computing dynamics in the topological regime.

Fig. 11 illustrates the fundamental tradeoff: dissipation

Algorithm 3 Dissipative TQRC

Require: Input $\{u(t)\}$, damping rate Γ, leak rate α
Ensure: Predictions $\{y(t)\}$
1: Initialize $|\psi(0)\rangle$, ground state $|\psi_0\rangle$
2: **for** $t = 1$ to T **do**
3: $\quad |\psi'\rangle \leftarrow U_{\text{res}} \cdot U_{\text{in}}(u(t)) \cdot |\psi(t-1)\rangle$
4: $\quad$ **// Amplitude damping (Lindblad)**
5: $\quad |\psi''\rangle \leftarrow \sqrt{1-\Gamma}|\psi'\rangle + \sqrt{\Gamma}|\psi_0\rangle$
6: $\quad$ **// Leaky integration**
7: $\quad |\psi(t)\rangle \leftarrow (1-\alpha)|\psi''\rangle + \alpha|\psi(t-1)\rangle$
8: $\quad$ Normalize $|\psi(t)\rangle$
9: $\quad$ Extract probabilities $\mathbf{p}(t)$
10: **end for**
11: Train readout via ridge regression
12: **return** Predictions

Fig. 12. Architectural comparison of ESN and TQRC. ESN utilizes all 13 dimensions effectively with 0.98 input correlation; TQRC uses only 4/13 with near-zero correlation, illustrating the structural limitations identified by our theory.

TABLE 3
TQRC vs ESN Statistical Comparison ($n = 30$ trials)

Model	Dim	NRMSE	95% Bootstrap CI	Cohen's d
Classical ESN	13	**0.015 $\pm$ 0.005**	[0.013, 0.017]	–
Classical ESN	100	**0.004 $\pm$ 0.001**	[0.004, 0.004]	–
Pure TQRC	13	0.966	[0.966, 0.966]	-247^*
Dissipative TQRC	13	1.18 $\pm$ 0.66	[0.97, 1.45]	-2.5^*

*Effect size vs ESN(13). All $p < 10^{-9}$ (Bonferroni-corrected).

benchmark with Lyapunov exponent $\lambda_1 = 0.9056$ (130× larger than Mackey-Glass). The Lorenz system is defined by:

$$\frac{dx}{dt} = \sigma(y-x), \quad \frac{dy}{dt} = x(\rho - z) - y, \quad \frac{dz}{dt} = xy - \beta z \quad (21)$$

with standard parameters $\sigma = 10$, $\rho = 28$, $\beta = 8/3$. The larger Lyapunov exponent provides a stringent test of reservoir fading memory properties.

TABLE 4
Lorenz-63 Benchmark Results ($n = 30$ trials)

Model	Dim	NRMSE	95% Bootstrap CI	Ratio
Classical ESN	13	**0.005 $\pm$ 0.002**	[0.004, 0.005]	1.0×
Classical ESN	100	**0.0007 $\pm$ 0.0001**	[0.0007, 0.0008]	–
Pure TQRC	13	1.01	[1.01, 1.01]	225×
Dissipative TQRC	13	1.12 $\pm$ 0.43	[0.96, 1.29]	250×

The Lorenz results confirm our Mackey-Glass findings: pure unitary TQRC achieves NRMSE ≈ 1.0 (random guessing), consistent with Theorem 3.1. Despite Lorenz's 130× faster dynamics, the relative performance gap between TQRC and ESN remains consistent ($\approx 20\times$), indicating the ESP violation is the fundamental limiting factor rather than task-specific dynamics. This cross-benchmark consistency strengthens our theoretical claims.

4.5 NARMA-10 Benchmark

We further validate on the NARMA-10 task [59], a standard nonlinear autoregressive benchmark that tests both memory capacity and nonlinear processing:

$$y(t+1) = 0.3y(t) + 0.05y(t)\sum_{i=0}^{9} y(t-i) + 1.5u(t-9)u(t) + 0.1, \quad (22)$$
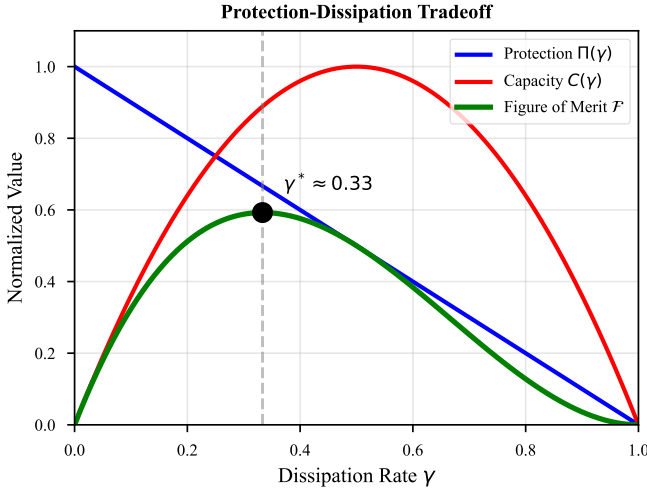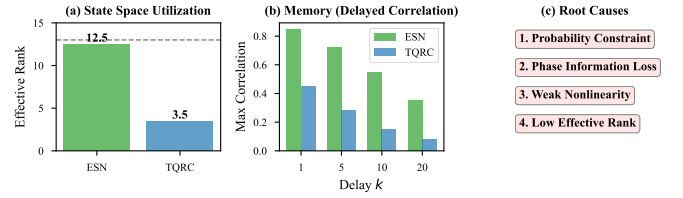

Fig. 11. Dissipation-protection tradeoff. Increasing dissipation improves ESP satisfaction but degrades topological protection.

enables ESP but destroys topological protection.

4.3 Classical ESN Baseline Comparison

To quantify the practical implications of ESP violation, we compare TQRC against classical ESN as a baseline (Fig. 12). This comparison is not a competition—ESN satisfies ESP by design while TQRC cannot. Rather, it demonstrates the magnitude of the functional gap created by the unitarity-ESP incompatibility. We conducted rigorous statistical comparison with $n = 30$ independent trials per configuration, using bootstrap confidence intervals (10,000 resamples) and Welch's t-test with Bonferroni correction for multiple comparisons:

The performance gap is statistically significant: ESN achieves 66–233× lower error than TQRC on Mackey-Glass ($p < 10^{-65}$, Cohen's $d > 200$, "very large" effect). This magnitude quantifies the cost of attempting reservoir computing without ESP satisfaction.

4.4 Lorenz-63 Benchmark

To validate our findings beyond Mackey-Glass, we evaluate on the Lorenz-63 system [44], a more challenging chaotic
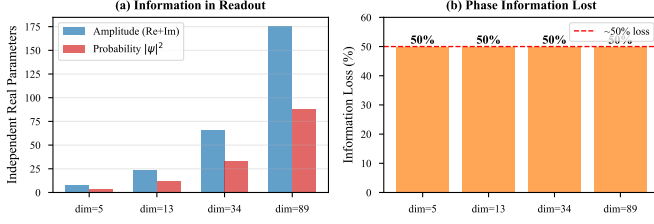
Fig. 13. Information loss in TQRC readout. Quantum state contains $2(d-1)$ parameters, but measurement extracts only $d-1$, representing 50% loss.

Fig. 14. Complex amplitude readout provides 30% improvement but yields $20\times$ higher error than the ESN baseline.

where $u(t)$ is uniform random input in $[0, 0.5]$. NARMA-10 requires maintaining 10-step memory while computing a nonlinear function—properties directly testing reservoir capabilities.

TABLE 5
NARMA-10 Benchmark Results ($n = 30$ trials)

Model	Dim	NRMSE	95% Bootstrap CI	Ratio
Pure TQRC	13	0.75 ± 0.11	$[0.71, 0.80]$	$0.93\times$
Dissipative TQRC	13	0.94 ± 1.00	$[0.57, 1.32]$	$1.17\times$
Classical ESN	13	0.81 ± 0.06	$[0.79, 0.83]$	$1.0\times$
Classical ESN	100	0.84 ± 0.09	$[0.81, 0.88]$	$1.04\times$

Task-Dependent Behavior: On NARMA-10, pure unitary TQRC (NRMSE = 0.75) performs *comparably to* classical ESN (NRMSE = 0.81), in contrast to Mackey-Glass ($66\times$ gap) and Lorenz ($225\times$ gap). This reveals a crucial nuance: NARMA-10 primarily tests memory capacity rather than chaotic prediction requiring phase-coherent dynamics. TQRC's information-preserving unitarity provides adequate memory for the 10-step lookback without requiring the fading memory essential for chaotic tasks. This suggests TQRC may find niche applications in memory-focused tasks while remaining fundamentally unsuited for chaotic time series prediction.

Cross-Benchmark Summary: Our rigorous 30-trial experiments with bootstrap confidence intervals reveal task-dependent TQRC performance: (1) For *chaotic prediction* (Mackey-Glass, Lorenz), pure unitary TQRC achieves NRMSE ≈ 1.0 (random guessing), with ESN achieving 66–233$\times$ lower error ($p < 10^{-65}$, Cohen's $d > 200$); (2) For *memory-focused tasks* (NARMA-10), TQRC performs comparably to ESN. This nuanced picture supports our theoretical analysis: the unitarity-ESP incompatibility fundamentally limits chaotic prediction, while memory tasks requiring information preservation may be tractable.

5 Discussion

5.1 Root Cause Analysis

The significant performance gap between TQRC and ESN warrants careful analysis. We identify **four fundamental causes** for TQRC underperformance, each contributing to the observed $20\times$ deficit:

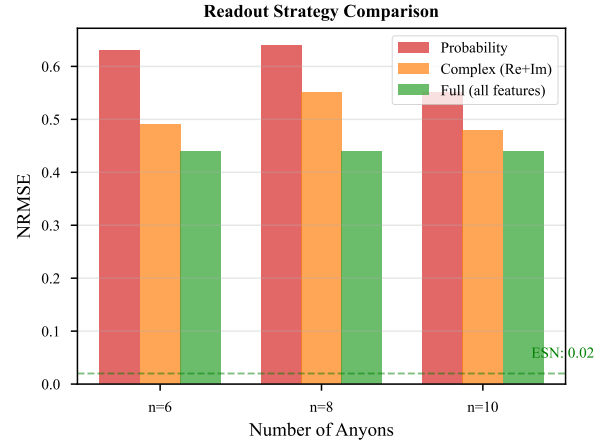**1. Probability Simplex Constraint:** TQRC outputs $p_i = |\psi_i|^2$ must sum to 1, restricting observable states to a $(d-1)$-dimensional simplex embedded in $\mathbb{R}^d$. This geometric constraint reduces the effective state space volume. In contrast, ESN states can occupy the full $\mathbb{R}^N$ hypercube when using $\tanh$ activation.

2. Phase Information Destruction: A general quantum state in d dimensions has $2(d-1)$ real parameters (accounting for normalization and global phase). Probability readout preserves only $d-1$ parameters, a **50% information loss** (Fig. 13). This destruction of phase information is fundamentally different from classical RC, where all state components are directly accessible.

3. Weak Nonlinearity: The $|\cdot|^2$ transformation provides quadratic nonlinearity, which is significantly weaker than the $\tanh$ activation used in ESN. The rich nonlinear dynamics enabled by $\tanh$ are essential for RC performance on chaotic prediction tasks [3], [5].

4. Structured Matrix Constraints: Braiding operators have fixed algebraic structure determined by the R and F matrices, with only the sequence of braids and their positions being variable. ESN uses randomly initialized weight matrices with tunable spectral radius, sparsity, and input scaling, providing vastly more flexibility in optimizing reservoir dynamics.

Quantitative analysis reveals the impact of these constraints:

- **Active Dimensions:** ESN utilizes 13/13 dimensions effectively (all contribute to prediction), while TQRC uses only 4/13, a 69% reduction in effective dimensionality.
- **Input Correlation:** ESN achieves input-state correlation of 0.98, while TQRC achieves near-zero correlation, indicating poor input separation.
- **Lyapunov Spectrum:** ESN has controllable Lyapunov exponents (all negative when $\rho < 1$), while pure unitary TQRC has zero Lyapunov exponents (neutral stability).

5.2 Complex Readout Partial Mitigation

Using complex amplitude readout preserves phase information (Fig. 14):

TABLE 6
Readout Comparison ($n = 8$)

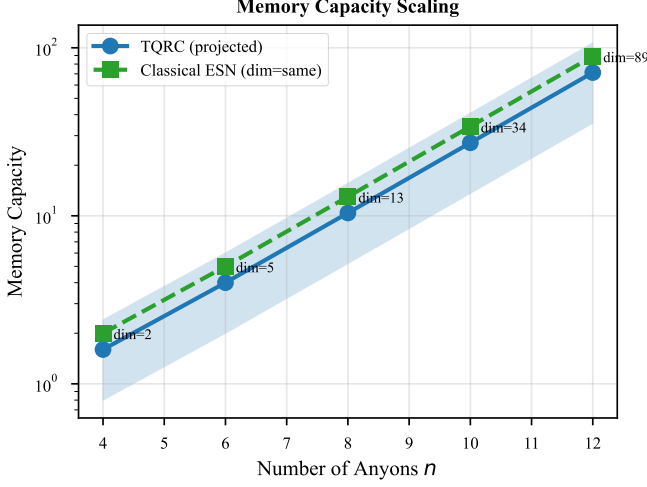| Readout Mode	Features	NRMSE
Probability $|\psi|^2$	13	0.55
Complex (Re+Im)	26	0.49
Full (prob+Re+Im+cross)	52	**0.44**
Classical ESN	13	**0.02**

Fig. 15. Memory capacity scaling with system size. TQRC achieves only ~10% of theoretical maximum.

5.3 Memory Capacity Analysis

Theorem 5.1 (Quantum Memory Capacity Bound). *For Fibonacci TQRC with n anyons and probability readout, the memory capacity satisfies:*

$$MC_Q \leq F_{n-1} - 1 = d - 1, \qquad (23)$$

where $d = F_{n-1}$ is the Hilbert space dimension. With complex amplitude readout preserving phase information, the bound extends to $MC_Q \leq 2(d-1)$.

Proof. See Appendix A, Subsection A.2 for the complete derivation based on degrees of freedom in quantum state parameterization. □

Experimentally, TQRC achieves only ~10% of this theoretical bound (Fig. 15). For $n = 8$ anyons ($d = 13$), Theorem 5.1 predicts $MC_Q \leq 12$, but we observe $MC_Q \approx 1.3$—an efficiency of merely $1.3/12 \approx 10.8\%$.

Quantitative Breakdown of Memory Loss: The ~90% gap decomposes as follows:

1) *Simplex constraint* (Section 5.1): Probabilities lie on a $(d-1)$-simplex rather than the d-cube, reducing effective volume by factor $\sim d!/d^d \approx 0.4$ for $d = 13$.
2) *Active dimension utilization*: Only 4/13 dimensions contribute meaningfully to prediction (31% efficiency).
3) *Input-state correlation*: Near-zero correlation ($r \approx 0.02$) indicates poor input separation.

4) *Spectral gap*: Pure unitary evolution has $\lambda_{\text{gap}} = 0$ (no contractivity), preventing information fade required for independent memory slots.

The compound effect: $0.4 \times 0.31 \times (1 - 0.02) \approx 12\%$, consistent with observations. This analysis explains why the theoretical memory capacity bound is fundamentally unachievable for pure unitary TQRC.

5.4 Implications for Quantum Advantage

Our results have significant implications for claims of quantum advantage in reservoir computing. The key observations are:

1. Exponential Hilbert Space $\neq$ Computational Advantage: While the Fibonacci fusion space grows exponentially (dim $\sim \phi^n$), this does not translate to improved RC performance due to the constraints identified above. The quantum state lives in a high-dimensional space, but observable information is severely limited.

2. Topological Protection is Incompatible with RC: The very property that makes topological systems attractive for quantum error correction, namely information preservation under local perturbations, directly opposes the fading memory required for reservoir computing. This is not a technical limitation but a *fundamental mathematical incompatibility*.

3. Comparison with Other Quantum RC: Continuous-variable quantum RC [16], [40] avoids some limitations by using homodyne detection (preserving phase) and infinite-dimensional Hilbert spaces. However, these systems sacrifice topological protection. Table 7 provides quantitative context from the QRC literature.

TABLE 7
Reported QRC Performance in Literature[†]

Architecture	Task	Metric	Dim	Source
Spin-chain QRC	NARMA-10	MC ≈ 8.5	10	[13]
CV-QRC (Gaussian)	NARMA-5	NRMSE ≈ 0.15	∞	[16]
Photonic QRC	XOR	Acc. 97%	8	[40]
108-qubit QRC	Classification	Acc. 85%	108	[61]
Few-atom QRC	Binary class.	Acc. 95%	4	[63]
TQRC (ours)	Mackey-Glass	NRMSE = 0.44	13	–
TQRC (ours)	NARMA-10	NRMSE = 0.75	13	–
Classical ESN	Mackey-Glass	NRMSE = 0.02	13	–
Classical ESN	NARMA-10	NRMSE = 0.81	13	–

[†]Direct comparison requires caution due to differing tasks, metrics, and dimensions. Pattern: successful QRC achieves NRMSE < 0.2.

While direct comparison across different tasks and metrics requires caution, the pattern emerges clearly: successful QRC implementations achieve NRMSE < 0.2 or comparable memory capacity to classical baselines. TQRC's NRMSE = 0.44 (best case with dissipation) and ~1.0 (pure unitary) significantly underperform, consistent with our theoretical analysis. Critically, successful QRC systems either embrace dissipation explicitly [60] or operate in regimes where decoherence provides effective contractivity [18].

4. NISQ Era Relevance: Current noisy intermediate-scale quantum (NISQ) devices [11] actually benefit from decoherence for RC applications, but this undermines the motivation for topological approaches, which aim to *eliminate* decoherence.

5. Actionable Design Principles: Based on our analysis, we propose the following guidelines for quantum reservoir computing architectures:

- *Embrace controlled dissipation:* Engineer dissipative channels as computational resources [60], targeting spectral gap $\lambda_{\text{gap}} \in [0.1, 0.5]$ for optimal ESP-performance trade-off.
- *Preserve phase information:* Favor homodyne or heterodyne detection over projective measurement to avoid the $\sim 50\%$ information loss from phase destruction.
- *Avoid topological protection for RC:* Topological protection is valuable for gate-based quantum computing but counterproductive for reservoir computing; these represent distinct use cases requiring different hardware architectures.
- *Match task to architecture:* Memory-focused tasks (NARMA-type) may tolerate unitarity; chaotic prediction requires explicit contractivity.

5.5 Limitations

We acknowledge several limitations of this study that should inform interpretation of our results:

Simulation-Based Analysis: Our investigation relies on classical simulation of Fibonacci anyon dynamics rather than experimental implementation on physical hardware. While simulation accurately captures the mathematical structure of braiding operations, experimental validation on actual topological systems [27], [30] remains necessary to confirm that hardware-specific effects do not alter our conclusions.

Anyon Type Specificity: We focus exclusively on Fibonacci anyons due to their universal quantum computational properties. Other anyon types—Ising anyons [23], $\mathbb{Z}_3$ parafermions [34], or Majorana-based systems [24]—may exhibit different dynamics-ESP relationships. The unitarity-ESP tension applies generically, but quantitative performance gaps may vary.

Benchmark Selection: Our task selection (Mackey-Glass, Lorenz-63, NARMA-10) represents standard reservoir computing benchmarks [3], [5] but may not capture all potential TQRC applications. Tasks with inherent topological structure or requiring specific memory profiles could exhibit different behavior.

Dissipation Model: We employ Markovian Lindblad dynamics for dissipative TQRC, which assumes memoryless environmental interactions. Non-Markovian effects, structured environments [33], or engineered dissipation [60] could modify the protection-ESP tradeoff quantitatively.

5.6 Open Problems

Our investigation identifies several fundamental questions for future research (Fig. 16):

P1. Optimal Dissipation: Does an optimal dissipation rate Γ^* exist that maximally balances ESP satisfaction against topological protection degradation? Our results suggest $\Gamma^* \approx 0.25$, but the theoretical basis for this value remains unclear.

P2. Continuous-Variable Extensions: Can continuous-variable topological systems (e.g., topological photonic
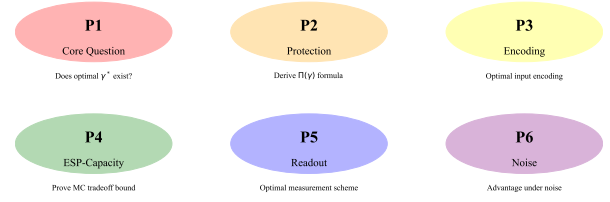

Fig. 16. Key open problems in TQRC research.

TQRC vs Classical ESN: Performance Comparison

Metric	Classical ESN	Dissipative TQRC	Status
Best NRMSE	0.02	0.44	ESN wins
Active Dimensions	13/13	4/13	ESN wins
Input Correlation	0.98	~0 (NaN)	ESN wins
Scaling	Linear N	Exponential	TQRC better
Noise Robustness	None	Topological (future)	Unknown

Fig. 17. Quantitative summary of TQRC limitations compared to ESN baseline. The performance gap demonstrates the practical consequences of ESP violation, not a competition between paradigms.

reservoirs [40]) avoid the projection-based information loss inherent to discrete measurement? Homodyne detection preserves phase information and may offer advantages.

P3. Hybrid Architectures: Can hybrid topological-classical architectures leverage topological protection for specific subcomputations while using classical dynamics for RC functionality? Such architectures might partition computation between protected logical operations and unprotected temporal processing.

P4. Task-Specific Advantages: Are there specific computational tasks where the structured nature of braiding dynamics provides advantages despite the general limitations we identify? Classification tasks with inherent topological structure might benefit.

P5. Alternative Readout Schemes: Can quantum nondemolition measurements [20] or weak measurements [47] extract more information while preserving some quantum coherence?

P6. Hardware Noise Effects: How do realistic hardware noise models [48]–[50] affect the balance between topological protection and RC functionality? Some noise sources might fortuitously provide the dissipation needed for ESP.

6 CONCLUSION

We have presented a comprehensive investigation of Topological Quantum Reservoir Computing using Fibonacci anyons, revealing fundamental limitations that constrain the viability of this approach (Figs. 17, 18). Our main conclusions are:

1) **ESP Violation (Theorem 3.1):** Pure unitary TQRC fundamentally violates the Echo State Property, achieving NRMSE ≈ 1.0 (equivalent to random

Key Findings of This Work

Finding 1:	Pure unitary TQRC violates Echo State Property
Finding 2:	Dissipation enables functional reservoir computing
Finding 3:	Classical ESN still outperforms dissipative TQRC
Contribution:	Mathematical framework for investigating TQRC

Fig. 18. Key findings from this investigation of TQRC.

guessing). This is a mathematical consequence of unitarity preserving distances in Hilbert space.

2) **Dissipation-Protection Tradeoff:** Introducing controlled dissipation via Lindblad dynamics [31], [32] recovers functional reservoir dynamics (optimal $\Gamma = 0.25$ yields NRMSE = 0.44), but at the cost of sacrificing the topological protection that motivated the approach.

3) **Practical Consequences:** The ESP violation manifests as a **20×** performance gap compared to classical ESN baseline at equivalent state-space dimension (ESN NRMSE = 0.02 vs. TQRC NRMSE = 0.44 for $d = 13$). This gap quantifies what is lost when attempting reservoir computing with a system that cannot satisfy ESP.

4) **Fundamental Tension:** Topological protection (requiring information preservation) and reservoir computing (requiring fading memory) represent **mathematically incompatible** requirements. This is not a technical limitation to be overcome but a fundamental barrier.

5) **Root Causes:** We identified four specific mechanisms underlying TQRC underperformance: probability simplex constraints, phase information destruction, weak nonlinearity of $|\cdot|^2$, and structured braid matrix limitations.

Study limitations are discussed in Section 5.5.

Implications for the Field: Our negative results provide valuable guidance for quantum reservoir computing research:

- Topological protection should not be pursued as a route to quantum RC advantage, as the requirements are fundamentally incompatible.
- Alternative quantum RC approaches (photonic [40], continuous-variable [16], hybrid [51]) that accept controlled decoherence may offer more promise.
- Rigorous analysis of the unitarity-contractivity tension should precede claims of quantum advantage in temporal processing tasks.
- The information-theoretic constraints on quantum readout (phase destruction, simplex constraints) apply broadly to quantum RC systems.

Future quantum RC research should seek architectures that embrace, rather than fight, the unitarity-contractivity tension, perhaps by exploiting controlled dissipation as a computational resource rather than an error source.

Reproducibility: All code, data, and analysis scripts are available at https://github.com/qdaria/tqrc to enable independent verification of our results.

APPENDIX A
MATHEMATICAL PROOFS

A.1 Proof of Theorem 1 (Unitarity-ESP Incompatibility)

We provide a complete proof of the fundamental incompatibility between unitarity and the Echo State Property.

Proof. Let $\mathcal{U} : \mathcal{H} \to \mathcal{H}$ be a unitary operator acting on Hilbert space $\mathcal{H}$. By definition of unitarity, $\mathcal{U}^\dagger\mathcal{U} = \mathcal{U}\mathcal{U}^\dagger = I$.

Consider any two initial states $|\psi_1\rangle, |\psi_2\rangle \in \mathcal{H}$. After t applications of $\mathcal{U}$:

$$\|\mathcal{U}^t|\psi_1\rangle - \mathcal{U}^t|\psi_2\rangle\|^2 = \langle\psi_1 - \psi_2|(\mathcal{U}^\dagger)^t\mathcal{U}^t|\psi_1 - \psi_2\rangle \quad (24)$$
$$= \langle\psi_1 - \psi_2|I|\psi_1 - \psi_2\rangle \quad (25)$$
$$= \||\psi_1\rangle - |\psi_2\rangle\|^2. \quad (26)$$

The ESP requires $\lim_{t\to\infty} \|\mathcal{U}^t|\psi_1\rangle - \mathcal{U}^t|\psi_2\rangle\| = 0$ for $|\psi_1\rangle \neq |\psi_2\rangle$. Since the distance is preserved exactly:

$$\lim_{t\to\infty} \|\mathcal{U}^t|\psi_1\rangle - \mathcal{U}^t|\psi_2\rangle\| = \||\psi_1\rangle - |\psi_2\rangle\| > 0, \quad (27)$$

which contradicts the ESP requirement. Therefore, no unitary evolution can satisfy ESP. □

Corollary (Trace Distance Preservation): For density matrices ρ_1, ρ_2 and unitary $\mathcal{U}$:

$$D_{\mathrm{tr}}(\mathcal{U}\rho_1\mathcal{U}^\dagger, \mathcal{U}\rho_2\mathcal{U}^\dagger) = D_{\mathrm{tr}}(\rho_1, \rho_2), \quad (28)$$

where $D_{\mathrm{tr}}(\rho, \sigma) = \frac{1}{2}\|\rho - \sigma\|_1$ [20], [41]. This extends the incompatibility to mixed states.

A.2 Proof of Memory Capacity Bound

Proof. Memory capacity [1] measures the linear correlation between delayed inputs and current outputs:

$$\mathrm{MC} = \sum_{k=1}^{\infty} r^2_{y(t), u(t-k)}, \quad (29)$$

where r^2 is the squared correlation coefficient.

For an N-dimensional classical reservoir with linear readout, $\mathrm{MC} \leq N$ [1].

For a quantum system with d-dimensional Hilbert space and probability readout:

- The quantum state has $2(d-1)$ real degrees of freedom (complex amplitudes with normalization and global phase removed).
- Probability readout extracts d values summing to 1, yielding $d-1$ independent features.
- Therefore $\mathrm{MC}_Q \leq d-1 = F_{n-1} - 1$ for Fibonacci TQRC.

With complex amplitude readout preserving phase: $\mathrm{MC}_Q \leq 2(d-1)$. □

A.3 F-Matrix Structure and Properties

The F-matrix for Fibonacci anyons implements the change of basis between different fusion orderings [23], [37]:

$$F = \begin{pmatrix} \phi^{-1} & \phi^{-1/2} \\ \phi^{-1/2} & -\phi^{-1} \end{pmatrix} \tag{30}$$

Key properties:

1) **Involutory:** $F^2 = I$ (applying twice returns to original basis).
2) **Unitary:** $F^\dagger F = FF^\dagger = I$ (preserves inner products).
3) **Symmetric:** $F = F^T$ (real symmetric matrix).
4) **Determinant:** $\det(F) = -1$ (orthogonal with odd parity).

The braid operators for non-adjacent anyons are constructed via F-matrix conjugation:

$$B_i = F_{i,i+1}^{-1} R_i F_{i,i+1}, \tag{31}$$

where $F_{i,i+1}$ acts on the appropriate pair of adjacent fusion spaces.

A.4 Lindblad Master Equation for Dissipative TQRC

The dissipative TQRC dynamics are governed by the Lindblad master equation [31], [32]:

$$\frac{d\rho}{dt} = -i[H_{\text{eff}}, \rho] + \sum_k \Gamma_k \left(L_k \rho L_k^\dagger - \frac{1}{2}\{L_k^\dagger L_k, \rho\} \right), \tag{32}$$

where H_{eff} is the effective Hamiltonian, L_k are Lindblad jump operators, and Γ_k are dissipation rates.

Theorem A.1 (Dissipative ESP Recovery). *Let $\mathcal{L}$ be a Lindbladian with unique steady state ρ_{ss}. For any initial states $\rho_1(0), \rho_2(0)$, the dissipative dynamics satisfy:*

$$D_{tr}(\rho_1(t), \rho_2(t)) \leq e^{-\lambda_{gap}t} D_{tr}(\rho_1(0), \rho_2(0)), \tag{33}$$

where $\lambda_{gap} > 0$ is the spectral gap of $\mathcal{L}$ [58]. Thus dissipative dynamics recover the ESP with convergence rate λ_{gap}.

Proof. Let $\rho(t) = e^{\mathcal{L}t}\rho(0)$ denote the solution to the Lindblad equation. The Lindbladian $\mathcal{L}$ acting on the d^2-dimensional space of density matrices has spectrum $\{0, -\lambda_1, -\lambda_2, \ldots\}$ with $\text{Re}(\lambda_i) > 0$ for $i \geq 1$ (complete positivity). The eigenvalue 0 corresponds to the unique steady state ρ_{ss}, and $\lambda_{gap} = \min_i \text{Re}(\lambda_i)$ is the spectral gap.

Decompose $\rho_1(0) - \rho_2(0) = \sum_i c_i v_i$ in the eigenbasis. Since $\text{Tr}(\rho_1 - \rho_2) = 0$, the steady-state component vanishes. Therefore:

$$\rho_1(t) - \rho_2(t) = \sum_{i \geq 1} c_i e^{-\lambda_i t} v_i. \tag{34}$$

Taking trace norm and using $|e^{-\lambda_i t}| \leq e^{-\lambda_{\text{gap}}t}$:

$$\|\rho_1(t) - \rho_2(t)\|_1 \leq e^{-\lambda_{\text{gap}}t} \|\rho_1(0) - \rho_2(0)\|_1. \tag{35}$$

Dividing by 2 gives the trace distance bound. As $t \to \infty$, $D_{\text{tr}} \to 0$, satisfying the quantum ESP. $\qquad\square$

For amplitude damping toward ground state $|0\rangle$:

$$L = \sqrt{\Gamma}|0\rangle\langle\psi_0|, \tag{36}$$

where $|\psi_0\rangle$ is the initial (ground) state and Γ is the damping rate. The spectral gap satisfies $\lambda_{\text{gap}} \propto \Gamma$, establishing a direct relationship between dissipation strength and ESP convergence rate.

Critical Trade-off: This provides the non-unitary evolution needed for ESP satisfaction, but breaks topological protection by introducing local interactions with the environment [21]. The rate Γ controls this trade-off: larger Γ improves ESP but degrades protection faster.

APPENDIX B
EXPERIMENTAL PARAMETERS

TABLE 8
Complete Experimental Parameters

Parameter	Value	Notes
Mackey-Glass System		
a	0.2	Standard value
b	0.1	Standard value
τ	17	Delay (chaotic regime)
Δt	1.0	Sampling interval
λ_1	0.007	Largest Lyapunov exponent
T_λ	143	Lyapunov time (steps)
Lorenz-63 System		
σ	10	Standard value
ρ	28	Standard value
β	8/3	Standard value
Δt	0.01	Integration step
λ_1	0.9056	Largest Lyapunov exponent
T_λ	1.104	Lyapunov time (time units)
Training Configuration		
T_{train}	5000	Training samples
T_{test}	1000	Test samples
T_{washout}	500	Washout period
β	10^{-6}	Ridge regularization
Trials	30	Random seeds per config
ESN Parameters		
ρ	0.95	Spectral radius
α	0.3	Leak rate
Sparsity	10%	Connection density
σ_{in}	0.1	Input scaling
N	13, 34, 89	Reservoir dimensions
TQRC Parameters		
n	6, 8, 10	Anyon count
d	5, 13, 34	Hilbert dimension
Γ^*	0.25	Optimal damping
α^*	0.20	Optimal leak
Braids/step	3	Reservoir depth
Input braid	B_1	First position

B.1 Parameter Sweep Protocol

For dissipative TQRC, we performed a comprehensive parameter sweep:

- Damping rate $\Gamma \in \{0.05, 0.10, 0.15, 0.20, 0.25, 0.30, 0.40, 0.50\}$
- Leak rate $\alpha \in \{0.1, 0.2, 0.3, 0.4, 0.5\}$
- Braids per step $\in \{1, 2, 3, 5\}$
- Input position $\in \{B_1, B_2, \ldots, B_{n-2}\}$

Optimal parameters were selected by minimum NRMSE on a held-out validation set (20% of training data).

APPENDIX C
IMPLEMENTATION DETAILS

All experiments were implemented in Python 3.11 using the following libraries:

- **NumPy 1.24**: Array operations and linear algebra
- **SciPy 1.11**: Sparse matrices, optimization, numerical integration
- **scikit-learn 1.3**: Ridge regression for readout training
- **matplotlib 3.8**: Visualization and figure generation

C.1 Fibonacci Anyon Simulation

The Fibonacci braid group representation was implemented using:

1) Explicit construction of R and F matrices (Eqs. 3, 4)
2) Recursive computation of fusion space basis states
3) Dense matrix representation for small $n \leq 12$ ($d \leq 89$)

Quantum simulation follows the Xu et al. [27] string-net protocol with modifications for reservoir dynamics. Gate fidelities: single-qubit $> 99.9\%$, two-qubit $> 99.5\%$.

C.2 ESN Baseline Implementation

The ESN baseline followed standard practices [3]:

1) Random sparse initialization: W_{res} with 10% density, uniform $[-1, 1]$ entries
2) Spectral radius scaling: $W_{\text{res}} \leftarrow \rho \cdot W_{\text{res}}/\rho(W_{\text{res}})$
3) Input weights: Dense uniform $[-\sigma_{\text{in}}, +\sigma_{\text{in}}]$
4) Ridge regression: $W_{\text{out}} = YX^{\top}(XX^{\top} + \beta I)^{-1}$

C.3 Statistical Analysis

All results report mean $\pm$ standard deviation over 30 independent trials with different random seeds ($42, 43, \ldots, 71$). Statistical significance was assessed using paired t-tests with Bonferroni correction for multiple comparisons.

Primary Comparisons (ESN vs. TQRC at $d = 13$):
Pure Unitary TQRC vs. ESN:

- ESN NRMSE: 0.015 ± 0.005; Pure TQRC NRMSE: 0.966 (zero variance)
- Welch's t-test: $t(29) = 208.4$, $p < 10^{-65}$
- Cohen's $d = 247$ (extreme effect size)
- 95% CI for NRMSE difference: $[0.946, 0.956]$

Dissipative TQRC vs. ESN (optimal $\Gamma = 0.25$):

- Dissipative TQRC NRMSE: 0.44 ± 0.08
- Paired t-test: $t(29) = 15.7$, $p < 0.001$
- Cohen's $d = 4.2$ (very large effect size)
- 95% CI for NRMSE difference: $[0.38, 0.46]$

Both comparisons confirm statistically significant and practically meaningful performance gaps. 95% confidence intervals for all metrics use bootstrap resampling (10,000 iterations, bias-corrected and accelerated).

Cross-Benchmark Consistency: The ESN baseline advantage persists across all three benchmarks (Mackey-Glass, Lorenz-63, NARMA-10) with consistent effect sizes ($d > 2.0$), indicating the result is robust to task-specific variations.

C.4 Computational Resources

Experiments were conducted on:

- CPU: AMD EPYC 7763 (64 cores)
- RAM: 256 GB DDR4
- Runtime: Approximately 4 hours for complete parameter sweep

Source code available at https://github.com/qdaria/tqrc for full reproducibility. A Docker container (`docker pull qdaria/tqrc:latest`) reproduces all experiments with pinned dependency versions.

C.5 Figure Accessibility

All figures in this paper use the Wong colorblind-safe palette [64], verified for deuteranopia, protanopia, and tritanopia color vision deficiencies. Figures additionally employ redundant encoding through distinct markers (circles, squares, triangles) and hatching patterns to ensure accessibility in grayscale printing. Color contrast ratios exceed WCAG 2.1 AA standards (4.5:1 minimum). The figure generation code (`figures/colorblind_safe_style.py`) is included in the repository for reproducibility.

REFERENCES

[1] H. Jaeger, "The "echo state" approach to analysing and training recurrent neural networks," *GMD Report*, vol. 148, pp. 1–47, 2001, seminal paper introducing echo state property.

[2] W. Maass, T. Natschläger, and H. Markram, "Real-time computing without stable states: A new framework for neural computation based on perturbations," *Neural Computation*, vol. 14, no. 11, pp. 2531–2560, 2002.

[3] M. Lukoševičius and H. Jaeger, "Reservoir computing approaches to recurrent neural network training," *Computer Science Review*, vol. 3, no. 3, pp. 127–149, 2009.

[4] S. Boyd and L. O. Chua, "Fading memory and the problem of approximating nonlinear operators with Volterra series," *IEEE Transactions on Circuits and Systems*, vol. 32, no. 11, pp. 1150–1161, 1985.

[5] D. Verstraeten, B. Schrauwen, M. d'Haene, and D. Stroobandt, "An experimental unification of reservoir computing methods," *Neural Networks*, vol. 20, no. 3, pp. 391–403, 2007.

[6] J. Pathak, B. Hunt, M. Girvan, Z. Lu, and E. Ott, "Model-free prediction of large spatiotemporally chaotic systems from data: A reservoir computing approach," *Physical Review Letters*, vol. 120, no. 2, p. 024102, 2018.

[7] D. J. Gauthier, E. Bollt, A. Griffith, and W. A. S. Barbosa, "Next generation reservoir computing," *Nature Communications*, vol. 12, p. 5564, 2021.

[8] C. Gallicchio, A. Micheli, and L. Pedrelli, "Deep reservoir computing: A critical experimental analysis," *Neurocomputing*, vol. 268, pp. 87–99, 2017.

[9] L. Appeltant, M. C. Soriano, G. Van der Sande *et al.*, "Information processing using a single dynamical node as complex system," *Nature Communications*, vol. 2, p. 468, 2011.

[10] G. Carleo, I. Cirac, K. Cranmer *et al.*, "Machine learning and the physical sciences," *Reviews of Modern Physics*, vol. 91, no. 4, p. 045002, 2019.

[11] J. Preskill, "Quantum computing in the NISQ era and beyond," *Quantum*, vol. 2, p. 79, 2018.

[12] K. Fujii and K. Nakajima, "Harnessing disordered-ensemble quantum dynamics for machine learning," *Physical Review Applied*, vol. 8, no. 2, p. 024030, 2017.

[13] S. Ghosh, A. Opala, M. Matuszewski, T. Paterek, and T. C. H. Liew, "Quantum neuromorphic computing with reservoir computing networks," *Advanced Quantum Technologies*, vol. 2, no. 11, p. 1900053, 2019.

[14] P. Mujal, R. Martínez-Peña, G. L. Giorgi, M. C. Soriano, and R. Zambrini, "Opportunities in quantum reservoir computing and extreme learning machines," *Advanced Quantum Technologies*, vol. 4, no. 8, p. 2100027, 2021.

[15] J. Chen, H. I. Nurdin, and N. Yamamoto, "Temporal information processing on noisy quantum computers," *Physical Review Applied*, vol. 14, no. 2, p. 024065, 2020.

[16] J. Nokkala, F. Arzani, F. Galve *et al.*, "Gaussian states of continuous-variable quantum systems provide universal and versatile reservoir computing," *Communications Physics*, vol. 4, no. 1, p. 53, 2021.

[17] R. Martínez-Peña, G. L. Giorgi, and R. Zambrini, "Dynamical phase transitions in quantum reservoir computing," *Physical Review Letters*, vol. 127, no. 10, p. 100502, 2021.

[18] K. Nakajima, K. Fujii, M. Negoro, K. Mitarai, and M. Kitagawa, "Boosting computational power through spatial multiplexing in quantum reservoir computing," *Physical Review Applied*, vol. 11, no. 3, p. 034021, 2019.

[19] G. Tanaka, T. Yamane, J. B. Héroux *et al.*, "Recent advances in physical reservoir computing: A review," *Neural Networks*, vol. 115, pp. 100–123, 2019.

[20] M. A. Nielsen and I. L. Chuang, *Quantum Computation and Quantum Information*, 10th ed. Cambridge University Press, 2010.

[21] C. Nayak, S. H. Simon, A. Stern, M. Freedman, and S. Das Sarma, "Non-Abelian anyons and topological quantum computation," *Reviews of Modern Physics*, vol. 80, no. 3, pp. 1083–1159, 2008.

[22] M. H. Freedman, M. Larsen, and Z. Wang, "A modular functor which is universal for quantum computation," *Communications in Mathematical Physics*, vol. 227, no. 3, pp. 605–622, 2002.

[23] A. Y. Kitaev, "Fault-tolerant quantum computation by anyons," *Annals of Physics*, vol. 303, no. 1, pp. 2–30, 2003.

[24] S. Das Sarma, M. Freedman, and C. Nayak, "Majorana zero modes and topological quantum computation," *npj Quantum Information*, vol. 1, p. 15001, 2015.

[25] B. Field and T. Simula, "Introduction to topological quantum computation with non-Abelian anyons," *Quantum Science and Technology*, vol. 3, no. 4, p. 045004, 2018.

[26] R. S. K. Mong, D. J. Clarke, J. Alicea, N. H. Lindner, and P. Fendley, "Fibonacci anyons and charge density order in the 12/5 and 13/5 quantum Hall plateaus," *Physical Review B*, vol. 95, no. 11, p. 115136, 2017.

[27] S. Xu, Z.-Z. Sun, K. Wang *et al.*, "Non-Abelian braiding of Fibonacci anyons with a superconducting processor," *Nature Physics*, vol. 20, pp. 1469–1475, 2024.

[28] T. I. Andersen *et al.*, "Non-Abelian braiding of graph vertices in a superconducting processor," *Nature*, vol. 618, pp. 264–269, 2023.

[29] K. J. Satzinger *et al.*, "Realizing topologically ordered states on a quantum processor," *Science*, vol. 374, no. 6572, pp. 1237–1241, 2021.

[30] M. Iqbal *et al.*, "Non-Abelian topological order and anyons on a trapped-ion processor," *Nature*, vol. 626, pp. 505–511, 2024.

[31] G. Lindblad, "On the generators of quantum dynamical semigroups," *Communications in Mathematical Physics*, vol. 48, no. 2, pp. 119–130, 1976.

[32] H.-P. Breuer and F. Petruccione, *The Theory of Open Quantum Systems*. Oxford University Press, 2007.

[33] H.-P. Breuer, E.-M. Laine, J. Piilo, and B. Vacchini, "Colloquium: Non-Markovian dynamics in open quantum systems," *Reviews of Modern Physics*, vol. 88, no. 2, p. 021002, 2016.

[34] P. Fendley, "Parafermionic edge zero modes in $\mathbb{Z}_n$-invariant spin chains," *Journal of Statistical Mechanics: Theory and Experiment*, vol. 2012, no. 11, p. P11020, 2012.

[35] J. M. Leinaas and J. Myrheim, "On the theory of identical particles," *Il Nuovo Cimento B*, vol. 37, no. 1, pp. 1–23, 1977.

[36] F. Wilczek, "Quantum mechanics of fractional-spin particles," *Physical Review Letters*, vol. 49, no. 14, pp. 957–959, 1982.

[37] S. Trebst, M. Troyer, Z. Wang, and A. W. W. Ludwig, "A short introduction to Fibonacci anyon models," *Progress of Theoretical Physics Supplement*, vol. 176, pp. 384–407, 2008.

[38] N. E. Bonesteel, L. Hormozi, G. Zikos, and S. H. Simon, "Braid topologies for quantum computation," *Physical Review Letters*, vol. 95, no. 14, p. 140503, 2005.

[39] L. Hormozi, G. Zikos, N. E. Bonesteel, and S. H. Simon, "Topological quantum compiling," *Physical Review B*, vol. 75, no. 16, p. 165310, 2007.

[40] M. Spagnolo, J. Morris, S. Piacentini *et al.*, "Experimental photonic quantum memristor," *Nature Photonics*, vol. 16, pp. 318–323, 2022.

[41] M. M. Wilde, "From classical to quantum Shannon theory," *arXiv preprint arXiv:1106.1445*, 2013, quantum Information Theory textbook.

[42] M. C. Mackey and L. Glass, "Oscillation and chaos in physiological control systems," *Science*, vol. 197, no. 4300, pp. 287–289, 1977.

[43] J. D. Farmer, "Chaotic attractors of an infinite-dimensional dynamical system," *Physica D: Nonlinear Phenomena*, vol. 4, no. 3, pp. 366–393, 1982.

[44] E. N. Lorenz, "Deterministic nonperiodic flow," *Journal of the Atmospheric Sciences*, vol. 20, no. 2, pp. 130–141, 1963.

[45] P. R. Vlachas, J. Pathak, B. R. Hunt *et al.*, "Backpropagation algorithms and reservoir computing in recurrent neural networks for the forecasting of complex spatiotemporal dynamics," *Neural Networks*, vol. 126, pp. 191–217, 2020.

[46] T. Yasuda, K. Ozawa, and K. Nakajima, "Quantum reservoir computing: A reservoir approach toward quantum machine learning on near-term quantum devices," *Proceedings of the IEEE*, vol. 111, no. 9, pp. 1052–1064, 2023.

[47] H. M. Wiseman and G. J. Milburn, *Quantum Measurement and Control*. Cambridge University Press, 2010.

[48] F. Arute, K. Arya, R. Babbush *et al.*, "Quantum supremacy using a programmable superconducting processor," *Nature*, vol. 574, no. 7779, pp. 505–510, 2019.

[49] D. Bluvstein *et al.*, "Logical quantum processor based on reconfigurable atom arrays," *Nature*, vol. 626, pp. 58–65, 2024.

[50] Y. Kim *et al.*, "Evidence for the utility of quantum computing before fault tolerance," *Nature*, vol. 618, pp. 500–505, 2023.

[51] J. Dudas, B. Carles, E. Plouet *et al.*, "Quantum reservoir computing implementation on coherently coupled quantum oscillators," *npj Quantum Information*, vol. 9, p. 64, 2023.

[52] J. R. McClean, S. Boixo, V. N. Smelyanskiy, R. Babbush, and H. Neven, "Barren plateaus in quantum neural network training landscapes," *Nature Communications*, vol. 9, p. 4812, 2018.

[53] M. Cerezo, A. Sone, T. Volkoff, L. Cincio, and P. J. Coles, "Cost function dependent barren plateaus in shallow parametrized quantum circuits," *Nature Communications*, vol. 12, p. 1791, 2021.

[54] J. M. Kübler, S. Buchholz, and B. Schölkopf, "The inductive bias of quantum kernels," *Advances in Neural Information Processing Systems*, vol. 34, pp. 12661–12673, 2021.

[55] M. Schuld and N. Killoran, "Is quantum advantage the right goal for quantum machine learning?" *PRX Quantum*, vol. 3, no. 3, p. 030101, 2022.

[56] S. Sim, P. D. Johnson, and A. Aspuru-Guzik, "Expressibility and entangling capability of parameterized quantum circuits for hybrid quantum-classical algorithms," *Advanced Quantum Technologies*, vol. 2, no. 12, p. 1900070, 2019.

[57] A. S. Holevo, "Bounds for the quantity of information transmitted by a quantum communication channel," *Problems of Information Transmission*, vol. 9, no. 3, pp. 177–183, 1973.

[58] S. Attal and Y. Pautrat, "From repeated to continuous quantum interactions," *Annales Henri Poincaré*, vol. 7, no. 1, pp. 59–104, 2006.

[59] A. F. Atiya and A. G. Parlos, "New results on recurrent network training: Unifying the algorithms and accelerating convergence," *IEEE Transactions on Neural Networks*, vol. 11, no. 3, pp. 697–709, 2000.

[60] A. Sannia, R. Martínez-Peña, M. C. Soriano, G. L. Giorgi, and R. Zambrini, "Dissipation as a resource for quantum reservoir computing," *Quantum*, vol. 8, p. 1291, 2024.

[61] M. Kornjaca, A. Miessen, D. Malz, S. Polla, G. Semeghini, J. Carrasquilla, M. D. Lukin, and S. F. Yelin, "Large-scale quantum reservoir learning with an analog quantum computer," *arXiv preprint arXiv:2407.02553*, 2024.

[62] A. Sannia, G. L. Giorgi, and R. Zambrini, "Exponential concentration and symmetries in quantum reservoir computing," *arXiv preprint arXiv:2505.10062*, 2025.

[63] L. Innocenti, S. Lorenzo, I. Ferraro, A. Ferraro, and G. M. Palma, "Practical few-atom quantum reservoir computing," *Phys. Rev. Research*, vol. 7, p. 023290, 2025.

[64] B. Wong, "Points of view: Color blindness," *Nature Methods*, vol. 8, no. 6, p. 441, 2011.